Perfect Resonant Absorption of Guided Water Waves by Autler-Townes Splitting

Léo-Paul Euvé, Kim Pham, Richard Porter, Philippe Petitjeans, Vincent Pagneux, Agnès Maurel

Perfect resonant absorption of guided water waves by Autler-Townes Splitting

L.-P. Euvé[1], K. Pham[2], R. Porter[3], P. Petitjeans[1], V. Pagneux[4], A. Maurel[5]
[1] *PMMH, ESPCI-PSL, Sorbonne Université, CNRS, 75005 Paris, France,*
[2] *LMI, ENSTA Paris, Institut Polytechnique de Paris, 91120, Palaiseau, France,*
[3] *School of Mathematics, University Walk, University of Bristol, Bristol, BS8 1TW, United Kingdom,*
[4] *LAUM, av. O. Messiaen, Le Mans Université, CNRS, 72085 Le Mans, France, and*
[5] *Institut Langevin, ESPCI-PSL, CNRS, 75005 Paris, France*

The control of guided water wave propagation based on the Autler-Townes Splitting (ATS) resonance concept is demonstrated experimentally, numerically and theoretically. Complete wave absorption is achieved using an asymmetric point-like scatterer made of two closely spaced resonant side channels connected to a guide and designed so that its energy leakage is in perfect balance with the inherent viscous losses in the system. We demonstrate that the nature of the resonators/guide junction completely controls the positions of the wavenumbers at the reflection and transmission zeros on the real axis; the asymmetry of the resonators completely controls their positions on the imaginary axis. Thus, by adjusting these two independent parameters, we obtain a zero reflection and transmission.

Wave phenomena being ubiquitous, the control of waves is an ever-changing field of study as displayed for instance in the last decades by the strong activity in metamaterials [1, 2]. Among the many wave controls that can be imagined, absorption is of particular interest since being able to lead to energy harvesting or noise cancellation. The perfect absorption (PA) of waves by compact devices poses a scientific and technological challenge that has attracted increasing interest in recent years, in optics [3–6], acoustics [7–12] and water waves [13–15]; in the latter context, this is motivated by the need to reduce the reflection of waves in harbours and basins [16, 17]. Achieving PA for reflective systems (one-port systems) is relatively easy as a single scattering coefficient, in reflection, is involved. It can be cancelled by using a scatterer whose resonance is critically coupled to the system [3, 6, 8, 13]. However, if transmission is allowed (two-port systems), obtaining perfect absorption becomes challenging because it requires the cancellation of both the reflection and transmission coefficients at the same frequency. A neat trick to get around this problem is to use two incident waves, one on each port, with a specific combination of incident amplitudes. A type of perfect absorption, called coherent perfect absorption (CPA), is thus obtained by reproducing the sum of two independent critical coupling problems [18, 19]. When waves are incident from one side, more sophisticated strategies have been devised using scatterers supporting two resonances. One strategy is to reduce the problem, in a non-symmetrical way, to a one-port problem with a resonator acting as a mirror over a certain frequency range [20–22]. Another strategy consists of activating, at the same frequency, two symmetric and antisymmetric resonances critically coupled to the system (degenerate resonances) [5, 23]. Coupled resonators resulting in electromagnetic induced transparency (EIT) in the lossless case have been as well shown to produce enhanced absorption [10].

In this study, we propose a new route to perfect absorption that is based on the Autler-Townes Splitting (ATS) concept. The ATS, like the EIT, originates from quantum physics. They correspond to limiting cases of strong or weak pumping in a three-level atomic system [24, 25], and their classical analogues have been analyzed [26–29]. In [30–32], it has been shown that two identical and closely spaced resonators attached to a guide behave as a point scatterer with monopolar and dipolar resonances leading to rapid variations in transmission and reflection. The appearance of ATS (two transmission zeros at separate, either real or complex conjugate, wavenumbers) has been analyzed for an increasing coupling between the resonators fostered by a strong evanescent field; for the classical EIT in contrast, the interaction is made possible by the interference of waves propagating between two resonators separated by a distance for which the evanescent coupling is negligible.

We consider two closely spaced resonant side channels connected to a waveguide in which water waves propa-

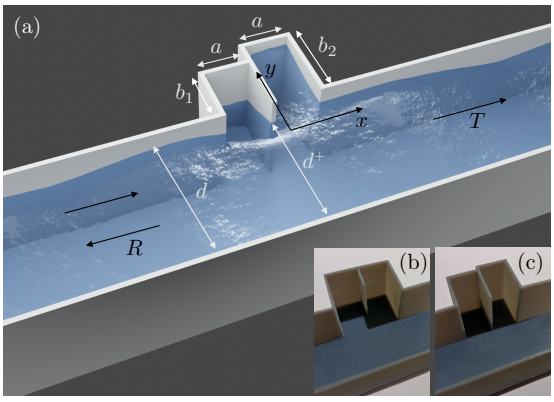

FIG. 1: (a) Conceptual view of the setting made of two closely spaced resonant channels (acting as a scatterer) connected to a guide where water waves propagate; the insets show pictures of the junctions made by 3D printing (b) a symmetric scatterer with $b_1 = b_2$ and (c) an asymmetric scatterer ($b_1 \neq b_2$) used for perfect absorption.

gate (figure 1). When the water depth h is constant a variation $\cosh k(z+h)$ in the depth coordinate z can be factorised from field variables and the resulting problem for the free surface elevation $\eta(x,y)$ becomes analogous to two-dimensional acoustics satisfying

$$\nabla^2\eta + k^2\eta = 0, \tag{1}$$

with dispersion $\omega^2 = gk\tanh kh$, (k the wavenumber at frequency ω and g the gravitational constant). In the following, the PA is going to be achieved by analyzing the wavenumbers at the zeros of transmission and reflection in the lossless case, which we want to drive to the same complex value, with the imaginary part exactly compensating the viscous losses induced by friction on the bottom and on the walls. To do this, we rely on the long-wavelength model of [32] which provides explicit expressions for the reflection and transmission coefficients. This allows us to interrogate the qualitative structure of the wave response and reveals the existence and nature of the ATS, thus providing an explicit recipe for tuning the system for PA. In parallel, we perform direct numerical calculations of the solution (i.e. without making any assumptions about long wavelengths, see Appendix A for details) and compare the results with experiments.

Analysis and experimental evidence of ATS. – To demonstrate the ATS mechanism, that is to say the strong evanescent coupling between the two resonators leading to two distinct zeros of transmission, we begin with the problem of a symmetric scatterer (two identical resonant side channels with heights $b = b_1 = b_2$ in figure 1), whose features will provide an important guide for the discussion of asymmetric scatterers (detuned side channels with $b_1 \neq b_2$). Note that evanescent coupling can be tuned by varying the ratio d^+/d, see Appendix B. The analysis that follows is made on the assumption of long waves equivalent to a low frequency approximation. Thus, in the guide, only the plane mode propagates and far enough away from the scattering region at $x = 0$, $\eta(x,y) \simeq \eta(x)$. For an incoming wave from the left with wavenumber k and complex amplitude $A^{\rm inc}$, the free surface elevation is $\eta(x) = A^{\rm inc}\left(e^{ikx} + R_0 e^{-ikx}\right)$, $x < 0$, and $\eta(x) = A^{\rm inc}T_0 e^{ikx}$, $x > 0$. with the time dependence convention $e^{-i\omega t}$ and with (R_0, T_0) the complex valued reflection and transmission coefficients. Following [32], the effect of the scatterer is replaced by jump conditions, at $x = 0$, on η and its derivative with respect to x; these jumps involve 4 real dimensionless parameters $(\delta_{\rm a}, \delta_{\rm s}, \delta_0, \delta)$ which depend only on the geometry of the junction d/a [32], with d the guide width and a the channel width, see figure 1; see also the §I of the Supplementary Material ($\rm SM_1$).

Close to the resonance frequency which occurs at $kb \sim \pi/2$, (R_0, T_0) can then be written

$$R_0 = -i\frac{a}{db}\,\frac{(k-\kappa_0)}{(k-k_0^+)(k-k_0^-)}, \quad T_0 = \frac{(k-\kappa_0^+)(k-\kappa_0^-)}{(k-k_0^+)(k-k_0^-)}, \tag{2}$$

where κ_0, $\kappa_0^\pm$ are the zeros of R_0 and T_0 and $k_0^\pm$ are the poles of the scattering matrix, which take the form

$$\begin{cases} \kappa_0 = \frac{\pi}{2b} - \frac{a}{b^2}\delta_{\rm a}, & \kappa_0^\pm = \frac{\pi}{2b} - \frac{a}{b^2}\left(\delta_0 \mp \sqrt{\Delta_0}\right), \\ k_0^- = \frac{\pi}{2b} - \frac{a}{b^2}\delta_{\rm s} - \frac{ia}{db}, & k_0^+ = \frac{\pi}{2b} - \frac{a}{b^2}\delta_{\rm a} - \frac{iad}{b^3}\delta^2, \end{cases} \tag{3}$$

with $\Delta_0 = (\delta_0 - \delta_{\rm a})^2 - \delta^2$. It can be remarked that the wavenumber κ_0 corresponding to zero reflection is always real, resulting in a transparent window in the transmission spectrum. In contrast, the wavenumbers $\kappa_0^\pm$ at the two transmission zeros experience a transition [33] from complex conjugates ($\Delta_0 < 0$) to purely real ($\Delta_0 > 0$) when increasing d/a. This is confirmed on figure 2 where we report results from direct numerics in the two-dimensional setting varying d/a and b/a at given a. We show the critical curve $(d/a)_c$ above which the wavenumbers at the zeros of T_0 are real. The insets (a-c) show typical profiles of $|R_0|$ and $|T_0|$ against wavenumber k, revealing the characteristic splitting of the two transmission zeros at real wavenumbers $\kappa_0^\pm$ as d/a is increased beyond $(d/a)_c$. Note that the model predicts that the critical curve $(d/a)_c$ ($\Delta_0 = 0$) is independent of the channel length b; numerically, we observe a dependence (albeit quite weak) with b that is not accounted for in the model (the model provides the asymptote $(d/a)_c = 1.8$ for large b/a).

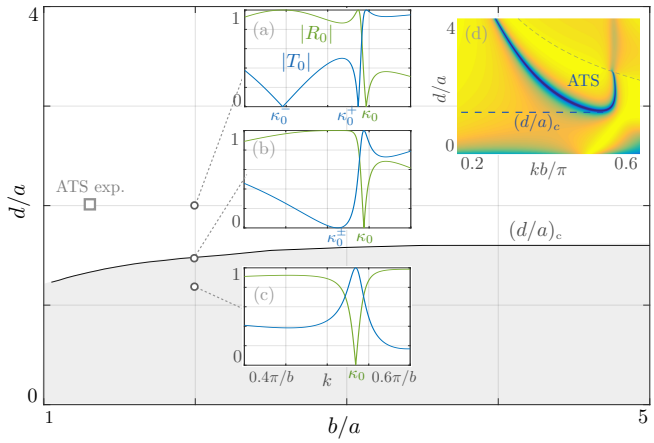

FIG. 2: Critical curve $(d/a)_c$ against b/a from direct numerics. (a-c): typical variations of (R_0, T_0) vs wavenumber k with two perfect transmission zeros at real wavenumbers $\kappa_0^\pm$ for $d/a > (d/a)_c$ and weak transmission dips for $d/a < (d/a)_c$. (d): Transmission spectrum for $b/a = 4/3$ as used in the ATS experiment.

In the experiment, we use $d = 6$ cm, $b = 4$ cm, $a = 3$ cm with a 140 cm long guide and a water depth $h = 5$ cm. Waves at frequencies $f \in (2.3, 3.7)$ Hz are generated using a plunging type wavemaker guided by a linear motor and placed at the left end of the guide (typical wavelength is 20 cm). We benefit from space-time resolved measurements from which, for each frequency, the complex field $\eta(x,y)$ can be deduced by Fourier transform of real time signals [34–36]; see Appendix C for

details. An example of such a field is shown in figure 3(a) for $f = 3.3$ Hz ($kb = 0.55\pi$). At this frequency, only the plane mode is propagating and, in the experiment, we observe that $\eta(x, y) \simeq \eta(x)$ in reflection and transmission except in the vicinity of $x = 0$. Here, the field is two-dimensional due to the presence of the evanescent field triggered by the junction. Therefore, we identify the complex incident amplitude $A^{\rm inc}$ and the scattering coefficients (R_0, T_0) by taking measurements far enough from this region (and in practice, $\eta(x)$ is obtained by averaging $\eta(x, y)$ over y). We also measure the complex amplitudes A_1 and A_2 on the end walls of the channels. Figure 3(b) shows the field radiated, or emitted, by the scatterer $\eta^{\rm rad}(x) = (\eta(x) - \eta^{\rm inc}(x))/A^{\rm inc}$ where $\eta^{\rm inc}(x) = A^{\rm inc}e^{ikx}$. We observe a symmetrical, monopolar, emission up to $f \simeq 3.1$ Hz, then a progressive phase shift of the transmitted wave leads to an asymmetrical, dipolar, emission. This is confirmed by the symmetric/antisymmetric amplitudes in the side channels, $A_s = (A_1 + A_2)$ and $A_a = (A_1 - A_2)$, whose variations as a function of f, normalized to $A = |A_1| + |A_2|$, are reported in figure 3(c). We observe that $|A_s|/A \simeq 1$ when the monopolar resonance is dominant ($A_1 \simeq A_2$ are in phase) and that $|A_a|/A \simeq 1$ when the dipolar resonance is dominant ($A_1 \simeq -A_2$ are out of phase).

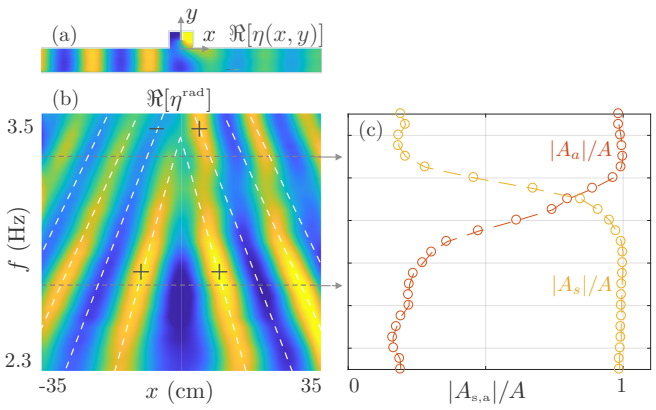

FIG. 3: Experimental ATS; monopolar and dipolar resonances – (a) $\Re[\eta(x, y)]$, the real part of $\eta(x, y)$, measured at $f = 3.3$ Hz. (b) Real part of the radiated field $\Re[\eta^{\rm rad}(x)]$ vs f revealing a transition from monopolar to dipolar resonances. (c) Normalized symmetric A_s and antisymmetric A_a channel amplitudes vs f ($A = |A_1| + |A_2|$).

The scattering coefficients $(|R_0|, |T_0|)$ as a function of frequency are shown in figure 4, highlighting the ATS with two dips in transmission (zero transmission in the lossless case). The monopolar resonance ($kb = 0.40\pi$) is very weakly affected by the losses, which leads to an almost zero transmission in good agreement with the direct numerics (dashed lines in the lossless case); on the other hand, the dipole resonance is significantly weakened with a transmission dip at $kb \simeq 0.55\pi$ which does not go to zero. In the model, the frequencies at monopole resonance ($\kappa_0^- b = 0.44\pi$) and at dipole resonance ($\kappa_0^+ b = 0.56\pi$) are consistent with our measure-

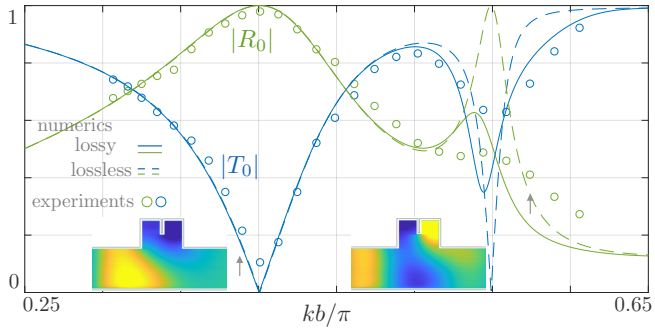

FIG. 4: Scattering coefficients vs non-dimensional wavenumber, experiments (symbols) and numerics (lossy case: plain line, lossless case: dashed lines). The insets show $\Re[\eta(x, y)]$ at $f = 2.7$ Hz and $f = 3.3$ Hz (arrows).

ments and each is associated with a near pole $k_0^{\pm}$ (with $k_0^- b = (0.46 - 0.16i)\pi$ and $k_0^+ b = (0.57 - 0.01i)\pi$. Furthermore, the leakage of the two resonances given by the imaginary parts of $k_0^{\pm}$ differ by a factor of 16, which is what we see in the experiment (when measuring for the two resonances, the ratio of the half-value widths or the absorption $\alpha = 1 - |R_0|^2 - |T_0|^2$) and what we used for the direct numerics in the lossy case shown by plain lines in figure 4. In doing so, however, we note mismatches between experiments and direct numerical calculations, which are partly attributable to imperfect modeling of the frequency dependence of losses in the experiments, and partly to unaccounted-for effects such as the nonlinearities inherent in the experiments.

Analysis and experimental realization of PA. – The PA is obtained by analyzing the wavenumbers associated with zero transmission and zero reflection in the lossless case, which we want to bring to the same complex value; this complex values will be compensated by the losses afterwards in the experiments [37]. According to what we have seen previously, this is not possible using a symmetrical scatterer because the wavenumber at zero reflection is always real. We will see that this is no longer the case for a non-symmetric scatterer; we now consider an asymmetry parameter ε defined by $b_1 = b(1 - \varepsilon)$, $b_2 = b(1 + \varepsilon)$, with $|\varepsilon| < 1$ (figure 1). Extending the model of [32] for different channel heights, we obtain near the resonance at $kb \simeq \pi/2$ the new form of the scattering coefficients

$$R = -i\frac{a}{db}\,\frac{(k-\kappa)}{(k-k^+)(k-k^-)}, \qquad T = \frac{(k-\kappa^+)(k-\kappa^-)}{(k-k^+)(k-k^-)}, \tag{4}$$

with

$$\kappa = \kappa_0 + i\,\frac{\pi d}{b^2}\delta\varepsilon, \qquad \kappa^{\pm} = \frac{\pi}{2b} - \frac{a}{b^2}\left(\delta_0 \mp \sqrt{\Delta}\right), \tag{5}$$

and $\Delta = \Delta_0 + \left(\frac{\pi b}{2a}\right)^2 \varepsilon^2$ (see SM$_1$). Compared to (3), we notice that the asymmetry shifts the wavenumbers at zero transmission; as we will consider a reference case

with $\Delta_0 < 0$, it only affects the imaginary part of $\kappa^{\pm}$. In parallel, the wavenumber at zero reflection acquires a complex value proportional to ε. We are now able to move to the PA without the need for a complex optimization process by performing $\kappa = \kappa^+$ (the zero of transmission with positive imaginary value) with two very simple steps: in step 1 we will first ensure equal real parts and subsequently in step 2 we will achieve equal imaginary parts.

Step 1: $\Re(\kappa) = \Re(\kappa^+)$ – If $\Delta < 0$ (which implies $\Delta_0 < 0$), this condition is the same as $\Re(\kappa_0) = \Re(\kappa_0^+)$ since the wavenumbers have a real part independent of ε. According to (3) and (5) this condition is realized when

$$\delta_0 = \delta_a. \tag{6}$$

Step 2: $\Im(\kappa) = \Im(\kappa^+)$ – This equality requires

$$\left(1 + \left(\frac{2\delta d}{b}\right)^2\right)\varepsilon^2 = \left(\frac{2\delta}{\pi}\frac{a}{b}\right)^2. \tag{7}$$

If we add the condition (6) on d/a, the above condition provides a one-to-one correspondence between (b/d) and $\varepsilon = \varepsilon_{\rm PA}$ realizing $\kappa = \kappa^+$, which is necessary to achieve perfect absorption when losses are taken into account.

To design our experimental setup, we followed the above procedure to obtain an initial guess and then used iterative test on experimental measurements which allows us to eventually find the values $a = 2.63$ cm, $b_1 = 3.24$ cm and $b_2 = 3.64$ cm ($\varepsilon = 0.058$) which fall very close to our prediction (see Appendix B). The PA is demonstrated and analyzed in figures 5 and 6. We first plot the field $\eta(x, y)$ measured at $f = 2.9$ Hz and the corresponding profile $\eta(x)$ averaged along y in the guide and normalized to the incident amplitude, see figure 5(a), where negligible transmission and reflection are realized. This is confirmed on figure 6(a) where we plot the variations of the (R, T) measured experimentally vs. kb/π; these variations are well reproduced by direct numerics using constant losses $k_i = 0.023$ cm^{-1}.

Perfect absorption is obtained because the scatterer is able to radiate strongly anisotropically (towards $x < 0$ and $x > 0$) in phase, which was already the case in the symmetric case but here also in amplitude. In figure 5(b), we have plotted $\eta^{\rm inc}(x)$ and $\eta^{\rm rad}(x)$ as functions of f, as in figure 3(a). The anisotropy is clearly visible and the conditions $\eta^{\rm rad}(x < 0) \simeq 0$ and $\eta^{\rm rad}(x > 0) \simeq -\eta^{\rm inc}(x > 0)$ are satisfied. This non-symmetric emission is made possible by a balance between the amplitudes A_1 and A_2 in the side channels, resulting in a balance between the symmetric A_s and antisymmetric A_a amplitudes shown in figure 6(b). We observe that these contributions are 90 degrees out-of-phase with a ratio $A_s/A_a \sim 0.5$ at the PA. Interestingly, this relationship is consistent with a calculation in which the two channels are replaced by two point sources separated by a distance $a/2$ and imposing amplitudes (A_1, A_2) with $A_1 = -A_2 e^{ika}$ (see SM$_2$).

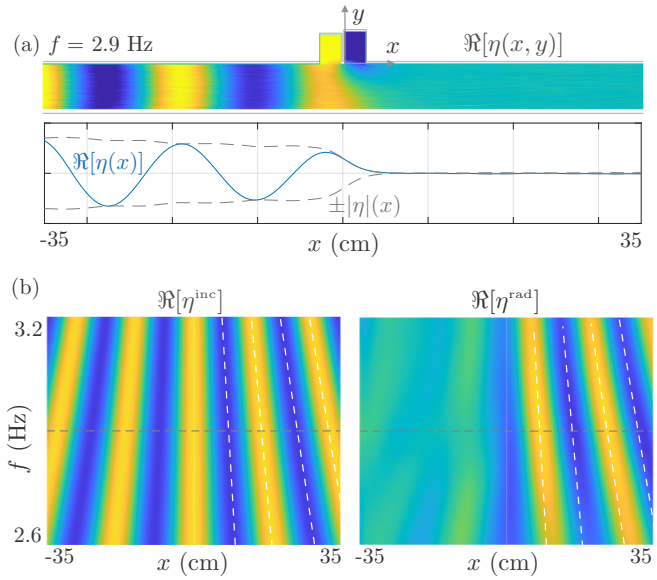

FIG. 5: Experimental measurements of the wavefield for the perfect absorption: (a) 2D field of the surface elevation $\eta(x, y)$ and mean profile $\eta(x)$ (real part and amplitude) at $f = 2.9$ Hz with no reflection (no beating of $|\eta|(x)$ for $x < 0$) and no transmission ($\eta(x) = 0$ for $x > 0$). (b) Profiles of the incident $\eta^{\rm inc}(x)$ and radiated $\eta^{\rm rad}(x)$ waves vs frequency.

In conclusion, we have demonstrated, experimentally and theoretically, the Autler-Townes splitting for a symmetric scatterer interacting with waves propagating in a guide. By extending the model to the case of non-symmetric scatterers, we have obtained a simple procedure to achieve perfect absorption by shifting, in the complex plane, the wavenumbers producing the transmission and reflection zeros to exactly the same value, chosen in such a way as to compensate exactly the inherent losses in the system. The approach we are following and the resulting phenomenology are not restricted to water waves, and thus, our findings could find applications to all the domains of wave physics, from matter to electromagnetic

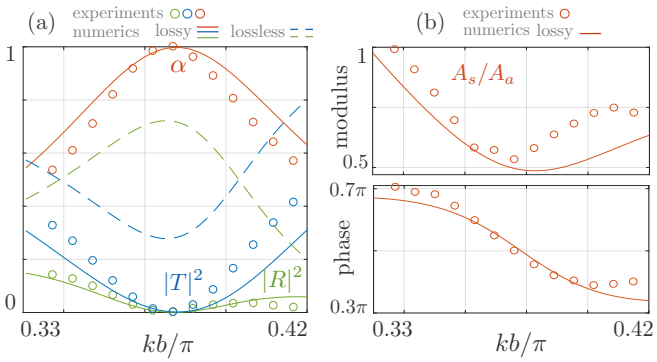

FIG. 6: Experimental PA – (a) Reflection $|R|^2$, transmission $|T|^2$ and absorption α against non-dimensional frequency kb/π. (b) modulus and phase of A_s/A_a.

and optical waves. We foresee that the proposed strategy, using asymmetric configuration of evanescently coupled resonators, opens new directions to achieve perfect subwavelength absorption; in particular, it would be interesting to extend our analysis to the case of a scatterer formed by $N > 2$ resonators with N governing the number of resonances.

Acknowledgements – The authors acknowledge the support of the ANR under grant 243560 CoProMM and ANR-19-CE08-0006, and of the Agence de l'Innovation de Défense from DGA under grant 2019 65 0070.

Appendix A : Numerical Method – Direct numerical calculations were performed by solving (1) using a multimodal method as in [32]. This consists of writing the two-dimensional field in each domain of constant width $d^{(j)} = (d, (d+b_1), d^+, (d+b_2), d)$, $j = 1, \cdots, 5$ in the form

$$\eta^{(j)}(x,y) = \sum_{n=0}^{\infty} \left(a_n^{(j)} e^{ik_n^{(j)} x} + b_n^{(j)} e^{-ik_n^{(j)} x} \right) E_n^{(j)}(y), \quad (8)$$

with the $E_n^{(j)}(y) = \cos(n\pi y/d^{(j)})$ forming a basis of transverse functions satisfying the boundary conditions at $y = 0$ and $d^{(j)}$ and the $k_n^{(j)} = \sqrt{k^2 - (n\pi/d^{(j)})^2}$ the wavenumbers along x. The problem is then solved classically by projecting the continuity conditions of η and $\partial_x \eta$ onto the transverse functions at each width discontinuity. The resulting system, after truncation of the series in (8), is then inverted to obtain the reflection coefficients $R_n = b_n^{(1)}$ (the incident wave being associated with $a_n^{(1)} = 1$), the transmission coefficients $T_n = a_n^{(5)}$ (with $b_n^{(5)} = 0$ which takes into account the radiation condition) and the amplitudes $(a_n^{(j)}, b_n^{(j)})$, $j = 2, 3, 4$, hence the whole complex field $\eta(x, y)$. In the lossy case, we simply consider $k = k_r + ik_i$. For the figure 4, we used $k_i b = 0.01\pi \exp\left[-\left(\frac{kb - 0.57\pi}{0.03b} \right)^2 \right]$, which produces the expected losses $k_i \simeq 10^{-3}$ cm^{-1} in the vicinity of the resonance at $k_r = 0.57\pi/b$. For the figure 6, we simply used contant k_i given by the imaginary part of κ.

Appendix B : Additional Informations on the ATS and PA experiments – The ATS experiments aims to demonstrate, for $b_1 = b_2$, the realization of two distinct transmission dips at two real wavenumbers (in the lossless case, two perfect transmission zeros). To do this, we used a junction region that foster evanescent coupling between the side channels; specifically communication between them was made easier by shifting the position of the partition wall, $d^+ > d$ as shown in the inset of figure 1(a) (we used $d = 6$ cm, $d^+ = 8$ cm for $a = 3$ cm). The resulting effective parameters $(\delta_a, \delta_s, \delta_0, \delta)$, which are independent of b and frequency, are for this *junction 1*: $\delta_a = -0.2831$, $\delta_s = 0.1501$, $\delta_0 = -0.0069$, $\delta = 0.1420$, resulting in $\Delta = \Delta_0 = 0.056 > 0$, according to the numerical results of the figure 1, slightly above the critical value $(d/a)_c \sim 1.6$ realizing $\Delta_0 = 0$ (in the model, this value is independent of b/a while the numerics shows a variation for small b/a values).

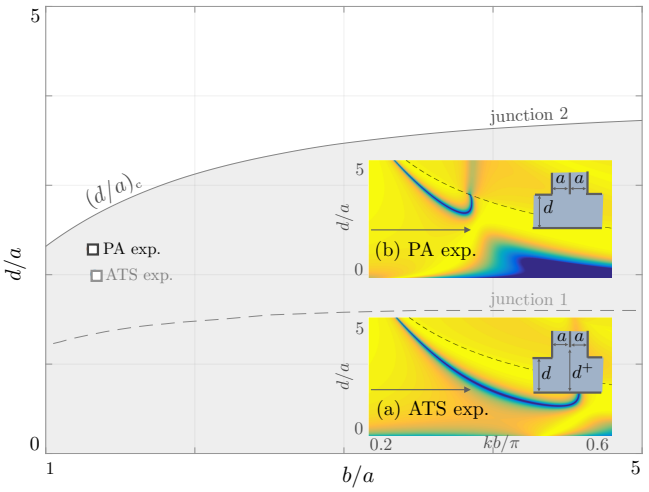

FIG. 7: Critical curves $(d/a)_c$ for the junction 1 (ATS exp.) and for the junction 2 (PA exp.) obtained from direct numerics. (a) shows the transmission spectrum for $b/a = 4/3$ as used in the ATS experiment, (b) shows the transmission spectrum for $b/a = 1.31$ as used in the PA experiment. In (a-b), we report the geometry of the junctions; $d/a = 3$ and $d^+/a = 4$ for the junction 1, $d/a = 2$ for the junction 2. The arrows show the values of d/a in the experiments.

In the PA experiments, we want complex wavenumbers at the transmission zeros, which, from (5), requires $\Delta_0 < 0$. As this condition implies small (d/a), which would increase losses due to viscous effects in the waveguide, we move to a junction (named junction 2) for which the partition wall is flush with the guide wall ($d^+ = d$). The numerically determined resulting critical curve $(d/a)_c$ is significantly shifted toward higher d/a values compared to that of junction 1, as shown in figure 7 (and, as for the junction 1, we observe a dependence of $(d/a)_c$ on b/a whereas the model only provides the asymptotic value $(d/a)_c = 3.7$ for large b/a, see [32]).

To design our experimental set-up, we start by following the two-step procedure (6)-(7) corresponding to the theoretical conditions of the PA. In the first step, (6) requires that $\delta_0 = \delta_a$ (which depends only on d/a, the junction geometry). We find that this condition is met for $d/a = 3.0$, which fixes the values of the 4 parameters, namely we have for this *junction 2* $\delta_a = \delta_0 = 0.6812$, $\delta_s = 0.6498$, $\delta = 0.2476$.
With $(d/a) = 3.0$ from the previous step, (7) provides a simple condition between b/d and ε only. The resulting curve $\varepsilon = \varepsilon_{PA}$ against b/d is shown in figure 8 (red dotted line). For completeness, we also show the shaded region (obtained numerically) within which the ATS with two distinct complex transmission zeros is observed. By construction, each pair $(b/d, \varepsilon)$ realizes $\kappa^+ = \kappa$, and we want now their imaginary part (in the lossless case) to be exactly compensated by the vis-

cous losses. In our experiments, we expect the losses to be well described by a wavenumber whose imaginary part is $k_i \in (0.02, 0.03)$ cm^{-1}. From (5), this reduces the allowable ranges along the $\varepsilon = \varepsilon_{\rm PA}$ curve to $b/d \in (0.55, 0.65)$ and $\varepsilon \in (6.3, 6.9)10^{-2}$. The inset in figure 8 shows the PA obtained numerically for a particular point of this curve for $k_i = 0.026$ cm^{-1} (the lossless case is shown for comparison) with an absorption reaching $\alpha = 1 - |R|^2 - |T|^2 \simeq 1$. As mentioned earlier, this analysis was used as a starting point in the experiments. The PA observed in figure 8 provides, if we use a waveguide with $d = 6$ cm, the values of $a = 2.0$ cm and $b_1 = 3.21$ cm, $b_2 = 3.67$ cm. We found that $a = 2.63$ cm, $b_1 = 3.24$ cm and $b_2 = 3.64$ cm produce higher absorption, as demonstrated in the main text (the □ in figure 8 which is close to the theoretical curve).

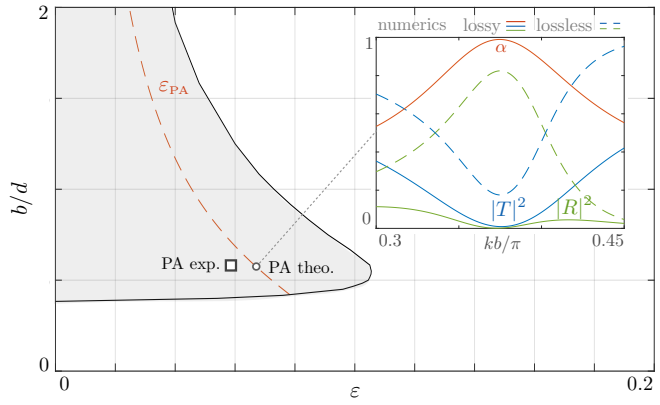

FIG. 8: PA for $\varepsilon = \varepsilon_{\rm PA}$ against b/d (dashed red line from (5)). Outside the shaded region, ATS takes place resulting in real valued $\kappa^{\pm}$. For $b/d = 0.57$, PA is achieved theoretically at ∘ (PA theo.) and experimentally at □ (PA exp). The inset shows the numerical PA with $\alpha \simeq 1$.

Appendix C : Experimental FTP Measurement – This measurement technique is based on the analysis of local displacements of fringes projected onto the free surface at rest and disturbed by wave propagation, which allows a measurement of the real-valued free surface elevation $\eta_t(x, y, t)$ recorded by a high speed camera. The complex-valued free surface elevation $\eta(x, y)$ is then obtained by Fourier transform $\eta(x, y) = \int_0^{t_{\rm f}} \eta_t(x, y, t) e^{i\omega t} {\rm d}t,$, with ω the working frequency imposed by the wave generator and $t_{\rm f}$ corresponding to several $2\pi/\omega$ periods [34–36]. We use a camera with 1936× 1216 pixels, which gives a spatial resolution $\delta x = \delta y = 0.4$ mm/px on a 75 cm wide region of the guide (including the height of the guide and channels) and a temporal resolution given by the camera acquisition speed $\delta t = 50$ ms.

[1] N. Engheta and R. W. Ziolkowski, *Metamaterials: physics and engineering explorations* (John Wiley & Sons, 2006).
[2] R. V. Craster and S. Guenneau, *Acoustic metamaterials: Negative refraction, imaging, lensing and cloaking*, vol. 166 (Springer Science & Business Media, 2012).
[3] A. Yariv, IEEE Photonics Technology Letters **14**, 483 (2002).
[4] T. S. Luk, S. Campione, I. Kim, S. Feng, Y. C. Jun, S. Liu, J. B. Wright, I. Brener, P. B. Catrysse, S. Fan, et al., Physical Review B **90**, 085411 (2014).
[5] J. R. Piper, V. Liu, and S. Fan, Applied Physics Letters **104**, 251110 (2014).
[6] J. R. Piper and S. Fan, Acs Photonics **1**, 347 (2014).
[7] X. Cai, Q. Guo, G. Hu, and J. Yang, Applied Physics Letters **105**, 121901 (2014).
[8] P. Wei, C. Croënne, S. Tak Chu, and J. Li, Applied Physics Letters **104**, 121902 (2014).
[9] M. Yang, C. Meng, C. Fu, Y. Li, Z. Yang, and P. Sheng, Applied Physics Letters **107**, 104104 (2015).
[10] A. Merkel, G. Theocharis, O. Richoux, V. Romero-García, and V. Pagneux, Applied Physics Letters **107**, 244102 (2015).
[11] V. Romero-García, G. Theocharis, O. Richoux, A. Merkel, V. Tournat, and V. Pagneux, Scientific Reports **6**, 1 (2016).
[12] A. Maurel, J.-F. Mercier, K. Pham, J.-J. Marigo, and A. Ourir, The Journal of the Acoustical Society of America **145**, 2552 (2019).
[13] E. Monsalve, A. Maurel, P. Petitjeans, and V. Pagneux, Applied Physics Letters **114**, 013901 (2019).
[14] R. Porter, Applied Ocean Research **113**, 102724 (2021).
[15] B. Wilks, F. Montiel, and S. Wakes, Journal of Fluid Mechanics **941** (2022).
[16] H. Martins-Rivas and C. C. Mei, Journal of Fluid Mechanics **626**, 395 (2009).
[17] I. Theocharis, E. N. Anastasaki, C. I. Moutzouris, and T. Giantsi, Ocean Engineering **38**, 1967 (2011).
[18] Y. Chong, L. Ge, H. Cao, and A. D. Stone, Physical Review Letters **105**, 053901 (2010).

[19] W. Wan, Y. Chong, L. Ge, H. Noh, A. D. Stone, and H. Cao, Science **331**, 889 (2011).
[20] N. Jiménez, V. Romero-García, V. Pagneux, and J.-P. Groby, Scientific Reports **7**, 1 (2017).
[21] W. R. Sweeney, C. W. Hsu, S. Rotter, and A. D. Stone, Physical Review Letters **122**, 093901 (2019).
[22] S. Soleymani, Q. Zhong, M. Mokim, S. Rotter, R. El-Ganainy, and Ş. Özdemir, Nature Communications **13**, 1 (2022).
[23] V. Romero-García, N. Jiménez, J.-P. Groby, A. Merkel, V. Tournat, G. Theocharis, O. Richoux, and V. Pagneux, Physical Review Applied **14**, 054055 (2020).
[24] S. H. Autler and C. H. Townes, Physical Review **100**, 703 (1955).
[25] N. B. Delone and V. P. Krainov, Physics-Uspekhi **42**, 669 (1999).
[26] C. Garrido Alzar, M. Martinez, and P. Nussenzveig, American Journal of Physics **70**, 37 (2002).
[27] A. Abdumalikov Jr, O. Astafiev, A. M. Zagoskin, Y. A. Pashkin, Y. Nakamura, and J. S. Tsai, Physical Review Letters **104**, 193601 (2010).
[28] P. M. Anisimov, J. P. Dowling, and B. C. Sanders, Physical Review Letters **107**, 163604 (2011).
[29] G. Andersson, M. K. Ekström, and P. Delsing, Physical Review Letters **124**, 240402 (2020).
[30] Y. Jin, Y. Pennec, and B. Djafari-Rouhani, Journal of Physics D: Applied Physics **51**, 494004 (2018).
[31] Y. Liu, A. Talbi, O. Bou Matar, P. Pernod, B. Djafari-Rouhani, et al., Physical Review Applied **11**, 064066 (2019).
[32] R. Porter, K. Pham, and A. Maurel, Physical Review B **105**, 134301 (2022).
[33] Y. Kang, A. Z. Genack, et al., Physical Review B **103**, L100201 (2021).
[34] A. Maurel, P. Cobelli, V. Pagneux, and P. Petitjeans, Applied Optics **48**, 380 (2009).
[35] P. J. Cobelli, A. Maurel, V. Pagneux, and P. Petitjeans, Experiments in fluids **46**, 1037 (2009).
[36] A. Przadka, B. Cabane, V. Pagneux, A. Maurel, and P. Petitjeans, Experiments in fluids **52**, 519 (2012).
[37] V. Romero-García, G. Theocharis, O. Richoux, and V. Pagneux, The Journal of the Acoustical Society of America **139**, 3395 (2016).